



Ultrahigh coulombic efficiency electrolyte enables Li||SPAN batteries with superior cycling performance

Haodong Liu¹, John Holoubek¹, Hongyao Zhou¹, Amanda Chen¹, Naijen Chang¹, Zhaohui Wu¹, Sicen Yu¹, Qizhang Yan¹, Xing Xing¹, Yejing Li¹, Tod A. Pascal^{1,2,*}, Ping Liu^{1,2,*}

¹ Department of NanoEngineering, University of California San Diego, 9500 Gilman Drive, La Jolla, CA 92093, USA

² Sustainable Power and Energy Center, University of California San Diego, 9500 Gilman Drive, La Jolla, CA 92093, USA

Raising the coulombic efficiency of lithium metal anode cycling is the deciding step in realizing long-life rechargeable lithium batteries. Here, we designed a highly concentrated salt/ether electrolyte diluted in a fluorinated ether: 1.8 M LiFSI in DEE/BTFE (diethyl ether/bis(2,2,2-trifluoroethyl)ether), which realized an average coulombic efficiency of 99.37% at 0.5 mA cm⁻² and 1 mAh cm⁻² for more than 900 cycles. This electrolyte also maintained a record coulombic efficiency of 98.7% at 10 mA cm⁻², indicative of its ability to provide fast-charging with high cathode loadings. Morphological studies reveal dense, dendrite free Li depositions after prolonged cycling, while surface analyses confirmed the formation of a robust LiF-rich SEI layer on the cycled Li surface. Moreover, we discovered that this ether-based electrolyte is highly compatible with the low-cost, high-capacity SPAN (Sulfurized polyacrylonitrile) cathode, where the constructed Li||SPAN cell exhibited reversible cathode capacity of 579 mAh g⁻¹ and no capacity decay after 1200 cycles. A cell where a high areal loading SPAN electrode (>3.5 mAh cm⁻²) is paired with only onefold excess Li was constructed and cycled at 1.75 mA cm⁻², maintaining a coulombic efficiency of 99.30% for the lithium metal. Computational simulations revealed that at saturation, the Li-FSI complex forms contact ion pairs, with a first solvation shell comprising DEE molecules, and a second solvation shell with a mix of DEE/BTFE. This study provides a path to enable high energy density Li||SPAN batteries with stable cycling.

Introduction

Long-life rechargeable batteries have enabled a mobile society and hold the promise of powering a future dominated by renewable energy generation and storage. However, ensuring the ubiquity of more demanding applications such as electric vehicles require cell energy densities far beyond those typically achievable today (<300 Wh kg⁻¹), and recently roadmaps to a cell energy density of 500 Wh kg⁻¹ have been discussed [1,2]. The deployment of lithium metal anodes is crucial to achieve this

goal, where achieving high coulombic efficiency is the defining limitation.

To this end, and regardless of the choice of cathode, developing lithium metal anodes that maintain stable long-cycling behavior remains a monumental challenge. The high reactivity of lithium metal towards most Li salts and organic solvents, paired with dendritic growth and dramatic surface area and volume changes, can lead to rapid degradation of the cell [3–6]. Recent methods for improving lithium metal anode performance generally revolve around addressing one or more of these fundamental issues: (1) designing electrolytes with new compositions [4,7–14]; (2) protecting the surface of the lithium anode via arti-

* Corresponding authors.

E-mail addresses: Pascal, T.A. (tpascal@eng.ucsd.edu), Liu, P. (piliu@eng.ucsd.edu).

ficial coatings [15–18]; and (3) constructing 3D porous hosts for uniform Li deposition [5,19–21].

Here we focus on electrolyte design, where the basic principle is to minimize parasitic reactions with lithium through the preferential formation of a robust solid electrolyte interface (SEI). One well-known method to achieve such an SEI is to employ electrolytes with high fluorine content. Of note, Fan et al. reported an all-fluorinated electrolyte which promoted the formation of a stable fluoride rich SEI and led to a coulombic efficiency (CE) of 99.2% at a current density of 0.2 mA cm^{-2} [7]. Another previously demonstrated method to improve SEI stability is to employ electrolytes with high salt concentrations, in which all available solvent molecules are coordinated by lithium ions, reducing their reactivity [22]. In this regard, Qian et al. demonstrated that a 4 M LiFSI–DME (lithium bis(fluorosulfonyl)imide in 1,2-dimethoxyethane) electrolyte provided a CE of 99.1% at a current density of 0.2 mA cm^{-2} , where the CE of a 1 M LiFSI–DME system was unstable under the same conditions [23]. To improve the transport properties while maintaining the lithium cycling behavior of such concentrated systems, Chen et al. proposed a localized high concentration electrolyte by implementing bis(2,2,2-trifluoroethyl) ether (BTFE), a non-solvent for lithium salts, as a diluent into a 5.5 M LiFSI–DMC (dimethyl carbonate) solution [8]. This electrolyte contained only 1.2 M LiFSI bulk concentration and demonstrated a record CE value of 99.5% at 0.5 mA cm^{-2} . The CE values decreased with increasing current densities, however, to 98.9% at 3 mA cm^{-2} and 92.6% at 5 mA cm^{-2} , respectively. The same group replaced the main solvent DMC by TEP (triethyl phosphate) to improve the safety of the electrolyte, which presents similar Li metal performance [24]. We note that for practical battery applications, high CE values are desired at current densities of at least $1.5\text{--}5 \text{ mA cm}^{-2}$, which would correspond to a 1C rate for electrode capacity loadings of $1.5\text{--}5 \text{ mAh cm}^{-2}$.

In this work, ether-based localized high-concentration fluorine-rich electrolytes (LHCFRE) are designed and investigated with various solvating ethers. Our justification for exploring such systems is as follows: (1) ethers are among the most stable polar solvents towards lithium metal, and (2) the high availability of FSI[−] in addition to fluorine-rich solvents should promote the formation of LiF as a dominant SEI component. In testing these design principles, we evaluated LHCFREs based on 1,3-dioxolane (DOL), 1,2-dimethoxyethane (DME), and diethyl ether (DEE). We demonstrate that a 1.8 M LiFSI/DEE (diethyl ether)–BTFE (weight ratio 1:4) “LDEE” electrolyte is the most promising, achieving a CE of 99.5% at 0.5 mA cm^{-2} for more than 900 cycles (3600 hours of testing). Furthermore, the LDEE system maintained a CE of 98.7% at 10 mA cm^{-2} , which promises to provide fast charging with the most aggressive of cathode loading metrics. This performance was found to be a result of a LiF-rich SEI layer, formed as a consequence of LiFSI decomposition on the lithium metal surface prior to the solvent. Computational simulations revealed that the Li-FSI complex forms contact-ion pairs in the saturated solution with diethyl ether as the primary solvating species, and the BTFE molecules primarily residing in the second solvation shell, prioritizing the reactivity of BTFE and FSI[−] against Li.

In addition to high anode efficiency, the electrolyte also has to be compatible with the cathode of choice, where a lower operating voltage is preferred in ether-based electrolytes due to their limited oxidative stability. Hence, we have applied the LDEE system to the high-capacity SPAN (Sulfurized polyacrylonitrile) cathode, which yielded significantly improved cycling performance indicative of their compatibility despite its instability in common ether-based electrolytes due to the generation of soluble polysulfides. Hence, the LDEE electrolyte was found to simultaneously provide high CE for lithium metal and eliminate the dissolution of SPAN. These features were applied to a Li||SPAN cell, which exhibited no capacity decay after 1200 cycles at a current density of 0.5 mA cm^{-2} and cathode loading of 1.0 mAh cm^{-2} , providing a viable path for realizing a long-life, high specific energy Li||SPAN battery.

Experimental methods

Electrolyte preparation

The solvent ethylene carbonate (EC), diethyl carbonate (DEC), 1,3-dioxolane (DOL), 1,2-dimethoxyethane (DME) were purchased from Gotion and used as received. The diethyl ether (DEE), bis(2,2,2-trifluoroethyl)ether (BTFE), and Lithium bis(fluorosulfonyl)imide (LiFSI) were purchased from Sigma Aldrich. The six electrolytes of 1 M LiFSI/EC-DEC (1:1, w/w), 1 M LiFSI/DOL-DME (1:1, w/w), 1 M LiFSI/DEE, 0.47 M LiFSI/DOL-BTFE (1:4, w/w), 1.8 M LiFSI/DEE-BTFE (1:4, w/w), and 2.54 M LiFSI/DME-BTFE (1.216:4, w/w) were prepared by dissolving predetermined amounts of LiFSI salt into mixed solvents and stirred to achieve stable and clear solutions. Here, 1 M is defined as 1 M salt dissolved into 1 kg of solvent.

Synthesis of SPAN materials and preparation of SPAN electrode

Polyacrylonitrile (Sigma-Aldrich, Mw = 150,000) and elemental sulfur (Sigma-Aldrich) were hand milled in a mortar with mass ratio of 1:4 to ensure homogeneous mixing. The mixed powders were heated in an argon filled tube furnace at $450 \text{ }^\circ\text{C}$ for 6 h with a ramp rate of $2 \text{ }^\circ\text{C}/\text{min}$, then cooled down to room temperature. According to the elemental analysis, the mass percentage of C, N, and S in SPAN are 39.51%, 14.58%, and 38.71%, respectively. SPAN cathode was prepared with SPAN powder, Super-P and PVDF in a ratio of 80:10:10 mixed in N-methyl pyrrolidinone (NMP) solvent and cast on Al foil. After drying in a vacuum oven at $80 \text{ }^\circ\text{C}$ overnight, the SPAN cathode was cut into 12 mm discs.

Electrochemical test

2032-type coin cells were used for all the electrochemical performance studies in this work. The Celgard $25 \text{ }\mu\text{m}$ trilayer PP-PE-PP membrane was used as a separator. One spring and one $500 \text{ }\mu\text{m}$ thick spacer was placed on the anode side under the Li electrode to match the thickness of the coin cell case. Fixed amount of electrolyte ($\sim 50 \text{ }\mu\text{L}$) was added into each coin cell to guarantee the completely wetting of the separator and electrodes.

For Li||Cu cell, the $250 \text{ }\mu\text{m}$ thick lithium was punched to 12.5 mm discs as the Li electrode, the $9 \text{ }\mu\text{m}$ thick Cu foil was punched to 15 mm discs as the Cu electrode. The accurate coulombic efficiency test follows the PNNL protocol [25]. Prior

to the test, a condition cycle was carried out on all the cells, in this step a Li film was first deposited onto the Cu foil at 0.5 mA cm^{-2} for 10 h, and then fully stripped to 1 V. Another Li film (5 mAh cm^{-2}) was deposited again at designed current density, only 1 mAh cm^{-2} capacity of Li film was stripped and plated for 10 cycles. Finally, the Li film was fully stripped to 1 V.

For Li||SPAN cell, the $250 \mu\text{m}$ thick lithium with diameter of 15.8 mm was used as the counter electrode, the SPAN electrodes was punched to 12 mm discs. Galvanostatic charge/discharge was conducted between 1 and 3 V.

Galvanostatic cycling was conducted on an LBT-5V5A battery tester (Arbin instruments) and Land battery tester. The cycled electrode was recovered by disassembling the coin cell. All the samples were washed with DME three times and dried in the glovebox antechamber under vacuum.

Characterizations

The morphology and thickness of the deposited Li metal film and 3D composite electrode were characterized using scanning electron microscopy (FEI Quanta 250 SEM). The sample was adhered to a double-sided carbon tape and placed on a specimen holder. The prepared sample was sealed in a laminate plastic bag inside the glovebox for transferring to the SEM. The approximate time of sample exposed to air (from a sealed environment to the SEM stage) was less than 3 s. XPS (Kratos Analytical, Kratos AXIS Supra) was carried out using Al anode source at 15 kV and all the peaks were fitted based on the reference C–C bond at 284.6 eV. All XPS measurements were collected with a $300 \text{ mm} \times 700 \text{ mm}$ spot size using a charge neutralizer during acquisition. Survey scans were collected with a 1.0 eV step size, and were followed by high resolution scans with a step size of 0.05 eV for C 1s, O 1s, and F 1s regions [26–29].

Computational methods

Simulation setup and description

Simulation cells of bulk BTFE (58 molecules) and DOL/DME/DEE (32 molecules), as well as an amorphous Li-FSI structure (64 molecules) were created according to the experimental bulk densities. Systems comprising LDOL/LDME/LDEE with 5, 22 and 34 Li-FSI molecules, representing the experimental saturation limits of 0.5 M, 1.8 M and 2.5 M respectively, were created and equilibrated as described below. The organic molecules were described using the OPLS-AA forcefield [30], the FSI molecules by Pádúa and coworkers [31], and the Lithium ions by Dang [32]. Following the suggestion of Dzubiella and coworkers [33], care must be taken to include electronic polarization effects in MD simulations of low dielectric constant solvents such as DEE and DME. Thus we scaled the partial atomic charges on the Li ion and FSI anion by 0.77, 0.726, 0.727, 0.757, 0.752 for pure BTFE, pure DME, pure DEE, LDEE and LDME respectively.

Molecular dynamics simulations

Equilibration molecular dynamics simulations were performed using the LAMMPS [34] code in order to generate ensemble structures for quantifying the Li-FSI solvation thermodynamics and structural parameters as a function of salt concentration. For each system, after an initial energy minimization at 0 K to obtain the ground state structure (energy and force tolerances of 10^{-4}),

the system was slowly heated from 0 K to room temperature at constant volume over 2 ns using a Langevin thermostat, with a damping parameter of 100 ps. The system was then subjected to 3 cycles of quench-annealing dynamics, where the temperature was slowly cycled between 298 K and 450 K over 4 ns. Annealing dynamics achieves faster equilibration in condensed phased systems because the system is given sufficient energy to overcome barriers on the potential energy surface and then allowed to relax to a lower energy valley.

After annealing, the system was equilibrated in the constant temperature (298 K), constant pressure (1 bar) or NpT ensemble for 5 ns. The temperature coupling constant was 0.1 ps while the pressure piston constant was 2.0 ps. The equations of motion used are those of Shinoda et al. [35], which combine the hydrostatic equations of Martyna et al. [36] with the strain energy proposed by Parrinello and Rahman [37]. The time integration schemes closely follow the time-reversible measure-preserving Verlet integrators derived by Tuckerman et al. [38]. The simulation cell lengths were monitored every 10 fs, with the average calculated from the last 2.5 ns of the NpT dynamics. The simulation cell was slowly changed to match these averages over a further 1 ns of dynamics. Finally, we performed 50 ns of constant volume, constant temperature (298 K) dynamics using the Nose-Hoover thermostat, with the same temperature coupling constant. Snapshots of the system (atomic coordinates and velocities) were saved every 1 ps for post-trajectory analysis. LAMMPS control and data files for each of the systems studied here are presented in the [supplementary materials](#).

Free energy calculations

Multi-stage free energy perturbation calculations were used to calculate the Li-FSI solvation free energy in each of the solvents/mixtures. Here, we write the potential energy of the system as:

$$U(\lambda) = U_{\text{bg}} + U_1(\lambda) + U_0(\lambda) \quad (1)$$

where U_{bg} in Eq. (1) is a background term corresponding to interaction sites whose parameters remain constant, U_0 is a reference term corresponding to the initial interactions of the atoms that will undergo perturbation, U_1 is a term corresponding to the final interactions of these atoms and λ is a coupling parameter, varying from 1 to 0 and thus connecting the fully interacting system to one where the LiFSI does not interaction with the solvent/mixture. The potential in Eq. (1) was implemented using standard λ -dependent soft-core Lennard-Jones potentials, as implemented in LAMMPS with $n = 1$ and $\alpha LJ = 0.5$. We calculated the solvation free energy by means of a stepwise alchemical transformations during a simulation run:

$$\Delta_0^1 A = \sum_{i=0}^{n-1} \Delta_{\lambda_i}^{\lambda_{i+1}} A = -kT \sum_{i=0}^{n-1} \ln \left\langle \exp \left(-\frac{U(\lambda_{i+1}) - U(\lambda_i)}{kT} \right) \right\rangle_{\lambda_i} \quad (2)$$

where the brackets in Eq. (2) indicate an ensemble average. We slowly varied λ in steps of 0.05 (22 steps in total, including the initial and final stages), where for each stage, we performed 500 ps of NpT dynamics at STP to equilibrate the system, followed by 1 ns of NpT dynamics for collecting statistics. We estimated the error in our calculated free energies at each stage by splitting the 1 ns production MD run into 4 sets of 250 ps runs and calculating

the statistical average and variance (standard deviation). The total variance was taken as the average of the variance at each stage. A separate FEP calculation was performed on an amorphous box of 64 LiFSI molecules, in order to obtain a correction to the solvation free energy arising from intra-FSI electrostatic interactions. Overall, these free energy calculations represent nearly 0.25 μs of simulation.

Entropy and self-diffusion constant calculations

Uncorrelated snapshots of the production MD simulation, 1 ns apart (a total of 25 separate calculations taking the last 25 ns of our NVT MD simulation), were subjected to a further 40 ps of NVT MD simulations, saving the atomic coordinates and positions every 2 fs. For each 40 ps trajectory, the entropy of the various molecules was calculated using an external code employing the Two-Phase Thermodynamics method [39,40], which evaluates the thermodynamics by utilizing atomic velocity autocorrelation functions (VACFs). The entropy of the various solution species (BTfE/solvent/Li/FSI) were evaluated separately by only considering the VACF of the relevant atoms. The self-diffusion constant of each of the species was also calculated within the same VACF approach, according to the rigorous Green–Kubo [41,42] statistical mechanical formulation. A C++ code implementing the 2PT method is available upon request from the authors.

Quantum chemistry calculations

Partial atomic charges and (HOMO/LUMO) energy levels of LiFSI molecules with an explicit first solvation shell, extracted from the molecular dynamics trajectories and pair distribution functions were calculated at the basis of density functional theory (DFT) level of theory using the Q-Chem 5.1 quantum chemistry package [43], and the B3LYP/aug-cc-PVTZ level of theory.

Results and discussions

The electrochemical stability of ether based localized high concentration electrolytes

First, we analyzed prospective LHCFRE solvating solvents by examining the Li cycling performance at dilute (1 M) salt concentrations in order to draw general conclusions regarding their reductive stability (Figs. S1–4). The coulombic efficiencies for lithium metal cycling was evaluated in Li||Cu coin cells by following the accurate coulombic efficiency test method, which is described in detail in the experimental methods [25]. The 1 M LiFSI/EC-DEC (EC-DEC) electrolyte showed a CE of 94.28% at 1 mA cm^{-2} (Fig. 1a), while the 1 M LiFSI/DOL-DME electrolyte delivered an improved CE of 98.69% at the same current density (Fig. S1). Due to severe lithium dendrite growth, the CE of EC-DEC decreases rapidly to 91.52% as the testing current density increases to 2 mA cm^{-2} , eventually failing at 3 mA cm^{-2} as a result of hard short (Fig. S4). Due to the evident superiority of ethers for Li stability, the same testing regimen was applied to 1 M LiFSI/DEE, which exhibited a high CE of 99.23% at 1 mA cm^{-2} (Fig. S1), indicating its promise for subsequent study in LHCFRE systems.

According to our previously stated design principles, DOL, DME, and DEE were chosen for the LHCFRE to examine the effects of salt concentration and solvation structure on the

lithium metal CE. The CE values of 0.47 M LiFSI/DOL-BTfE (LDOL), 2.54 M LiFSI/DME-BTfE (LDME), and 1.8 M LiFSI/DEE-BTfE (LDEE) were investigated (Fig. 1a), which were determined to be the salt saturation limits at a fixed diluent:solvating solvent molar ratio of 2.20:1.35. At 0.5 mA cm^{-2} , the LDEE, LDME, and LDOL electrolyte exhibited high CEs of 99.50%, 99.11%, and 98.92%, respectively. Despite the somewhat comparable performance at low rate, the advantage of the LDEE electrolyte becomes clear at high current densities, where a >99% CE was maintained at 5 mA cm^{-2} , compared to 98.70% for LDME. At 10 mA cm^{-2} the LDEE electrolyte retained a CE of 98.70%, where all other investigated systems experienced a short (Figs. S5–7).

Another critical factor affecting the performance of a realistic battery system is the long-term lithium cycling stability in the electrolytes, which we tested by continuously plating/stripping a Li||Cu cell in the LDEE electrolyte at 0.5 mA cm^{-2} with a capacity of 1 mAh cm^{-2} (Fig. 1b). Generally, tens of cycles is required to establish a stable SEI on Cu for high efficiency lithium metal cycling, a proposition that is problematic when applied to full-cells applying limited Li. For example, a previous study demonstrated a lithium CE of 99%, but only after 200 cycles [44]. The LDEE electrolyte, on the other hand, was found to reach a CE of 99% after only 15 cycles. After this initial improvement, the cell lasted more than 3600 h without shorting with an average CE of 99.37% over 900 cycles.

To further test the performance limits of the LDEE system, the high capacity deposition behavior of lithium was also investigated, where 5 mAh cm^{-2} was cycled repeatedly at 0.5 mA cm^{-2} (Fig. 1c). Under these conditions, the LDEE electrolyte exhibited an average CE of 99.40%, exceeding 99.0% CE after only 1 cycle. The plating/stripping voltage profiles of these tests can be found in Fig. 1d and e.

Before applying the DEE-based electrolytes to cathodes, the redox stabilities of LDEE were examined using cyclic voltammetry (CV) on Cu and Al electrodes, respectively. The LDEE electrolyte exhibited a lithium plating and stripping process with minimal polarization, in addition to the formation of SEI at 0.45 V. Upon scanning to positive potentials, an increase in current was observed at 4.1 V (Fig. S8), which places an upper bound of ~ 4.0 V on the voltage of perspective cathode materials. The conductivity was also measured by electrochemical impedance spectroscopy (Fig. S9), yielding an ionic conductivity of 2.1 mS cm^{-1} , which is comparable to previous LHCFRE systems [8,9,12]. As a comparison, the 9 M LiFSI/DEE showed a relatively lower conductivity of 1.8 mS cm^{-1} , indicating that the introduction of BTfE enhanced the conductivity of the high salt concentration electrolytes due to the reduced viscosity. The wettability tests showed that the 9 M LiFSI/DEE electrolyte cannot effectively wet the Celgard separator, whereas the BTfE diluted electrolyte can easily spread over and soak the Celgard separator (Fig. S10).

The chemistry at the interphase and Li anode morphology

XPS spectra were collected on the Li-plated Cu electrode on its 70th deposition to validate the chemistries at the interphase. Compositional analysis revealed that the SEI formed in 1 M LiFSI/DEE displayed F and C contents of 10.16% and 56.42% compared to that of the EC/DEC system at 4.58% and 68.15%

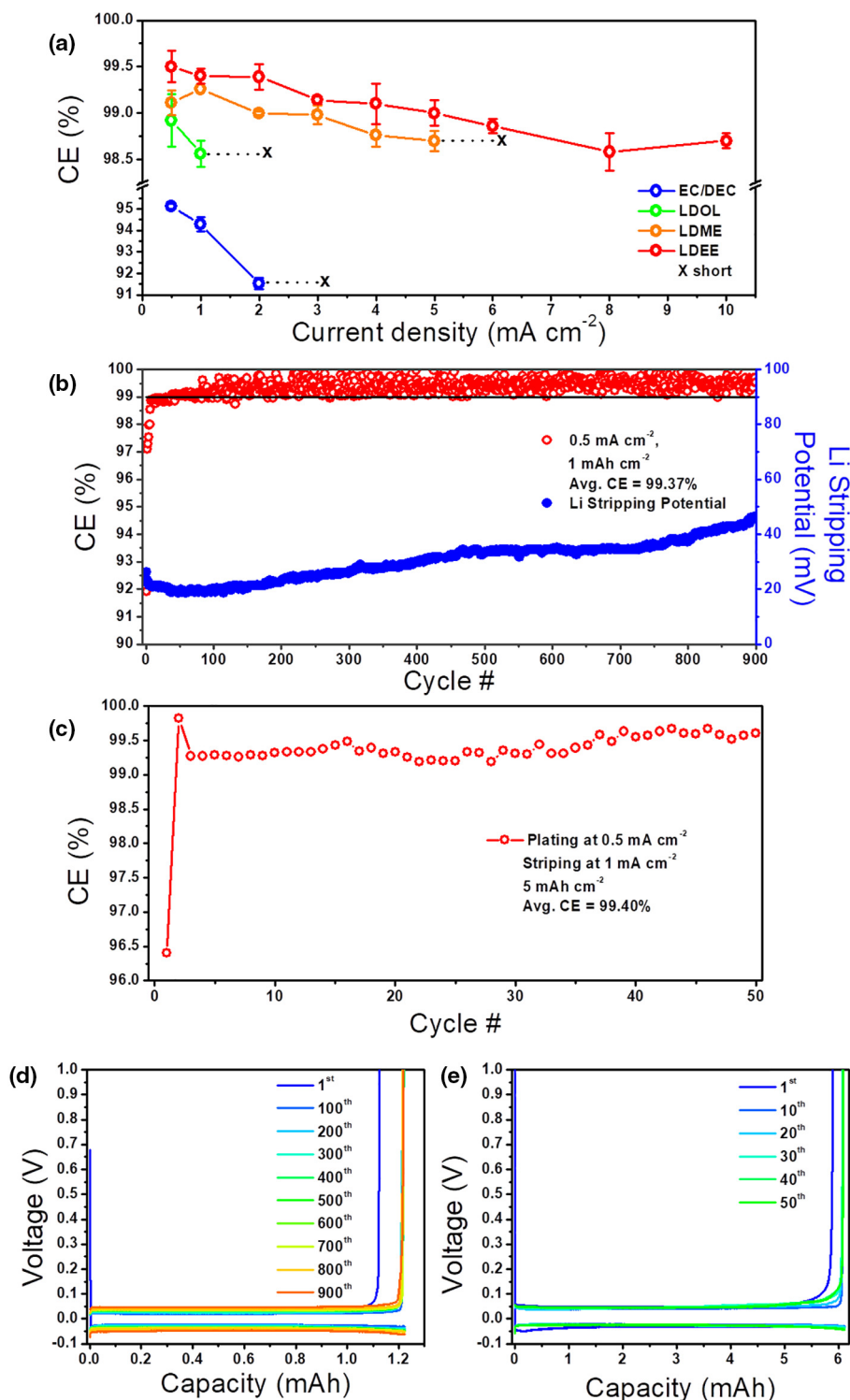


FIGURE 1

Li metal coulombic efficiency tests. (a) The comparison of Li-metal plating/stripping coulombic efficiencies in 1 M LiFSI/EC-DEC, 0.47 M LiFSI/DOL-BTFE, 2.54 M LiFSI/DME-BTFE, and 1.8 M LiFSI/DEE-BTFE electrolytes at various current densities. Coulombic efficiency of Li||Cu cell cycled in 1.8 M LiFSI/DEE-BTFE electrolyte at (b) 0.5 mA cm⁻² for 1 mAh cm⁻², and (c) plating at 0.5 mA cm⁻² and stripping at 1 mA cm⁻² for 5 mAh cm⁻². (d) The plating/stripping voltage profiles of Li||Cu cell cycled in 1.8 M LiFSI/DEE-BTFE electrolyte at (d) 0.5 mA cm⁻² for 1 mAh cm⁻², and (e) plating at 0.5 mA cm⁻² and stripping at 1 mA cm⁻² for 5 mAh cm⁻².

(Fig. 2a). The C 1s spectra exhibits the characteristic C-H, C-O, and C=O features at 284.6 eV, 286.0 eV, and 288.5 eV, respectively (Fig. S11) [10], which are present at a significantly reduced

intensity in the LDEE system, indicating the highly stabilized solvent molecules. The F 1s peaks at 684.8 eV, and 686.5 eV are assigned to the LiF, and S-F bond, respectively (Fig. 2) [45]. The

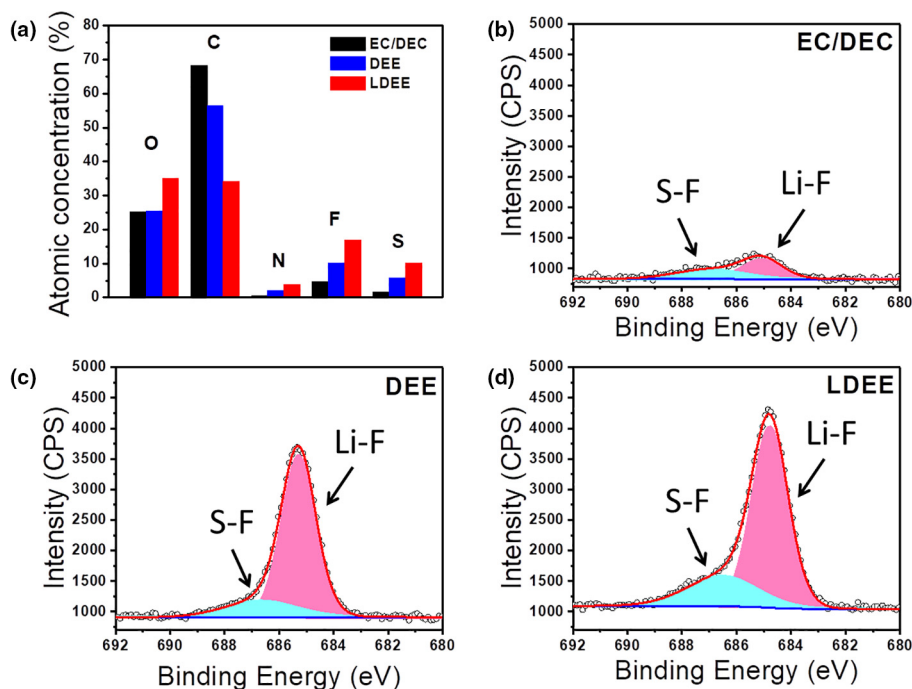


FIGURE 2

XPS analyses of Li plated on Cu after 70 cycles at 0.5 mA cm^{-2} for 1 mAh cm^{-2} . (a) Composition of SEI on the cycled Cu electrode in different electrolytes. F 1 s spectra of plated Li in (b) 1 M LiFSI/EC-DEC. (c) 1 M LiFSI/DEE. (d) 1.8 M LiFSI/DEE-BTFE.

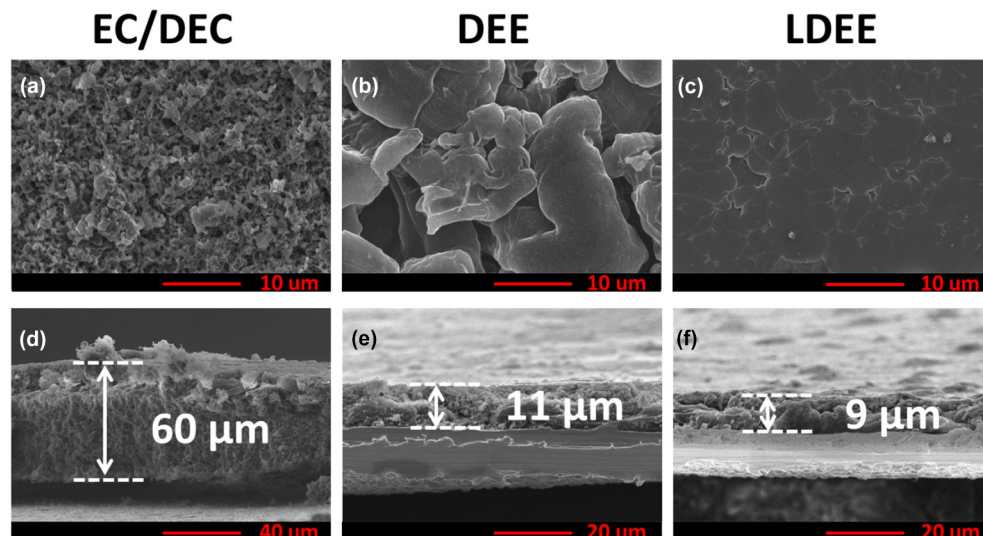


FIGURE 3

SEM images of Cu electrode on its 70th deposition. Top views: (a) Cu electrode from 1 M LiFSI/EC-DEC electrolyte. (b) Cu electrode from 1 M LiFSI/DEE electrolyte. (c) Cu electrode from 1.8 M LiFSI/DEE-BTFE electrolyte. Cross sectional views: (d) Cu electrode from 1 M LiFSI/EC-DEC electrolyte. (e) Cu electrode from 1 M LiFSI/DEE electrolyte. (f) Cu electrode from 1.8 M LiFSI/DEE-BTFE electrolyte. At 0.5 mA cm^{-2} for 1 mAh cm^{-2} .

fluorine content produced by the LDEE system was found to be significantly greater than that of the 1 M LiFSI/DEE electrolyte. In addition, the carbon content produced by the LDEE system was much less than that of the 1 M LiFSI/DEE electrolyte, which supports the conclusion that DEE is highly stabilized by the high salt concentration. We attribute these characteristics to the further increased presence of fluorine donors (LiFSI) and further sol-

vent stabilization by the high salt concentration, which likely plays a key role on promoting LiF formation, suppressing solvent decomposition, and regulating the metallic lithium growth [7].

In addition to the chemical analysis on SEI, the lithium deposition morphologies on Cu electrodes were also investigated (Fig. 3). According to theoretical calculations, 1 mAh cm^{-2} of 0 porosity lithium corresponds to a cross-sectional thickness of

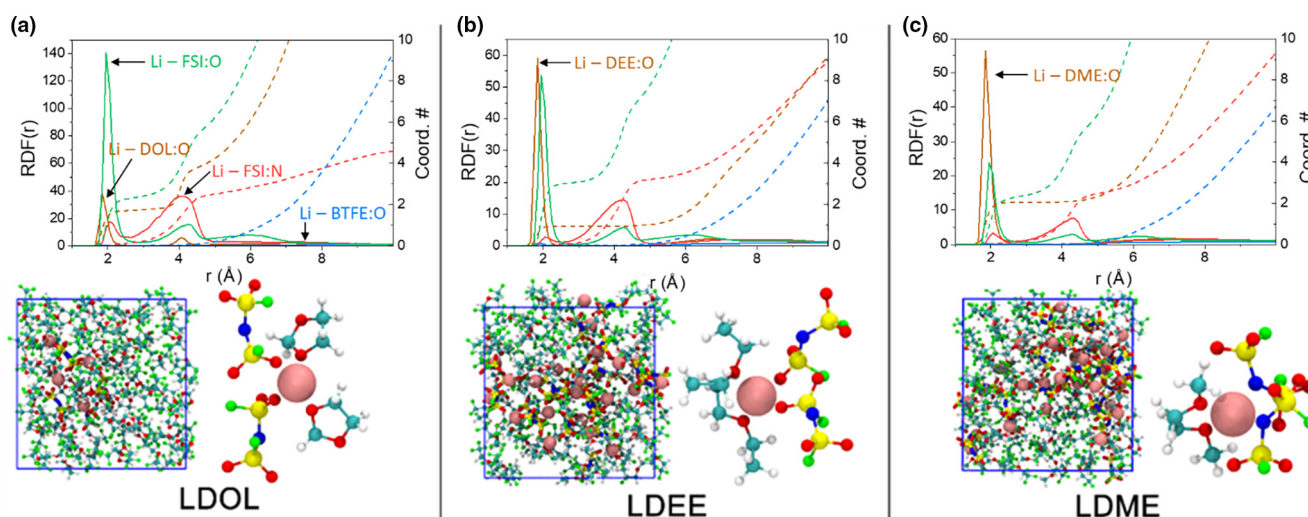


FIGURE 4

Computer simulation of Li-FSI solvation in various LHCFRE. (a) (*Top panel*) Pair distribution functions (PDFs) for a saturated solution (0.5 M LiFSI) of LDOL. Data for the Li – DOL:oxygen atom (solid brown line), Li – BTFE:oxygen atom (solid blue line), Li – FSI:nitrogen atom (solid red line), and FSI:oxygen atom (solid green line) are shown. Dashed lines are the integrated PDFs, representing the lithium coordination number (on right axis). (*Bottom left*) Final MD snapshot of the saturated LDOL solution, showing the BTFE (green) and solvated Li-FSI molecules (representative snapshot of 1st solvation shell shown in *bottom right* panel). (b and c) PDFs, final snapshots and representative solvation shell structure for 1.8 M LDEE and 2.5 M LDME respectively. Color: Li, pink; O, red; C, lightseagreen; H, white; N, blue; S, yellow; and F, green.

4.85 μm . The deposition of lithium in LDEE was found to be 5.5 μm , corresponding to a porosity of 12% after the first deposition (Fig. S12). This thickness was found to increase to 9 μm , 11 μm , and 60 μm after 70 cycles in LDEE, 1 M LiFSE/DEE, and 1 M LiFSI/EC-DEC, respectively. The EC/DEC system produced “needle-like” dendritic structures, indicative of a highly porous structure that yielded a low CE in the previous tests (Fig. S13). The investigation on the lithium morphologies confirmed that the dense Li deposition was maintained in LDEE electrolyte after long term cycling.

LHCFRE microstructure and solvation thermodynamics

To link the aforementioned performance metrics to the molecular properties of the electrolytes, the atomic morphology and thermodynamics of LiFSI salts dissolved in the various LHCFREs were explored by means of classical molecular dynamics (MD) simulations. Systems comprising 58 BTFE, 36 DOL/DME/DEE and Li-FSI salt molecules were created and subjected to ~ 100 ns of equilibration dynamics in order to access the equilibrium solution structure at the infinite dilution (i.e. 1 LiFSI salt molecule) and at the experimental saturation limits. At the saturation limit, our equilibrium MD simulations show the onset of salt agglomeration, and the formation of contact-ion pairs, in contrast to the solvent-separated ion pair in more dilute solutions. Analysis of the pair (radial) distribution functions (Fig. 4) for Li⁺ interacting with the FSI⁻ nitrogen and solvent oxygen atoms paint a consistent picture of the micro-solvation structure. In these saturated solutions, the oxygen atoms on the solvent at ~ 2 Å presents varied probabilities for Li⁺ interaction, where LDME was found to have the most Li⁺/solvent interaction, followed by LDEE, and finally LDOL, thus defining the first solvation shell of the three LHCFRE. Numerical integration reveals a

lithium environment comprising 2 DOL oxygens and 2 FSI⁻ in LDOL, 1.5 solvent oxygens and 2 FSI⁻ molecules in LDEE, and 2.5 solvent oxygens and 2 FSI⁻ molecules in LDME. Of note, there is a very low probability of finding a BTFE molecule in the 1st solvation shell (<1%). Indeed, the BTFE molecules are found to be on average ~ 8 Å away from the dissolved Li⁺. This is consistent with the experiment showing that LiFSI is insoluble in BTFE, and our free energy calculations, which find an unfavorable $+34.7 \pm 1.4$ kJ/mol solvation free energy of an isolated LiFSI in BTFE (Fig. S14). The solvation free energy of LiFSI in 1.8 M DEE (-10.8 ± 1.5 kJ/mol/molecule) is more favorable than in 1.8 M LDEE (-6.9 ± 2.8 kJ/mol/molecule) due to the unfavorable BTFE interaction in the latter. Moreover, our free energy calculations reveal that the LiFSI molecules are significantly more stable in 2.5 M LDME ($\Delta G_{\text{solv}} = -20.9 \pm 2.5$ kJ/mol/molecule) than in LDEE.

Rational basis for the electrode interphase structure

Our free energy calculations, and the relatively weak solvation free energy of LiFSI molecules in saturated LDEE solutions compared to DEE and LDME, suggests a mechanism for the preferential absorption of the FSI⁻ near the newly formed lithium surface during the lithium plating process. The close proximity of these anions near the metal interface, which is inversely related to the magnitude of the bulk solvation free energy, promotes electron transfer at reductive potentials and results in anion decomposition to form a stable SEI. Quantum chemistry calculations of solvated LiFSI molecules revealed that the LUMO of FSI⁻ is an anti-bonding state, with no electron density between the S-F and S-N bonds (Fig. S15). As such, assuming that the LUMO is occupied at reductive potentials, these bonds will be destabilized and likely cleave [22].

Li||SPAN full cell performance

While sulfur or metal oxide intercalation cathodes can both in principle achieve full-cell energy densities of 500 Wh kg^{-1} , sulfur-based cathodes are particularly appealing due to their low cost, abundant supply, and high storage capacity. Among these, the SPAN cathode is particularly promising due to the physical confinement of the small molecular sulfur in the conductive polymer network which provides a specific capacity of $>550 \text{ mAh g}^{-1}$ and an average discharge potential of $\sim 1.8 \text{ V}$ [46]. In addition, the dissolution-free solid-to-solid conversion mechanism shows promise to enable low-porosity, thick electrodes with stable cycling in lean electrolytes, provided that the selected solvents have limited polysulfide dissolution [47,48]. To evaluate our designed electrolyte systems in electrochemical cells, Li||SPAN cells were first assembled with a SPAN areal capacity of 1 mAh cm^{-2} . Since SPAN is well-known to be stable in carbonate electrolytes, the Li||SPAN cell was cycled in 1 M LiFSI/EC-DEC as the baseline between 1 V and 3 V at a current density of 0.5 mA cm^{-2} , which exhibited a high initial specific cathode capacity of 558 mAh g^{-1} , which slowly decreased to 453 mAh g^{-1} (81% retention) after 400 cycles (Fig. 5a) [49–51]. However, after the 480th cycle, the specific capacity was found to rapidly decay due to increased polarization (Fig. 5b), which is likely due to the degradation of the lithium anode and continuous consumption of the electrolyte given the low CE of the carbonate system.

By contrast, the 1 M LiFSI/DEE electrolyte, which showed promising CE for Li metal cycling yielded only 259 mAh g^{-1} by the 400th cycle (47% retention) (Fig. 5b). Such a result is consistent with Wei and coworkers, who showed that SPAN could dissolve in ethers, for example, in DOL/DME [49]. We investigated this by performing EDS measurements on SPAN that was

cycled in 1 M LiFSI/DEE 650 times, revealing a S/N ratio of 0.65 ± 0.12 (Fig. S16A) compared to the 0.95 ± 0.06 ratio found in pristine SPAN. These results indicate that while the 1 M LiFSI/DEE system provides sufficient Li CE, there is significant dissolution of SPAN which hinders the performance of the cell.

As shown by our previous computational results, the DEE molecules in the LDEE system are highly coordinated by Li^+ , hence LDEE was expected to dissolve little or no S. The same Li||SPAN cell in LDEE displays an initial activation, where the specific capacity increased rapidly from 426 mAh g^{-1} to 511 mAh g^{-1} within 5 cycles, afterwards gradually increasing to 579 mAh g^{-1} . After activation, the Li||SPAN cell exhibited (Fig. 5d) no capacity decay over 1200 cycles (5000 h of testing). Furthermore, the EDS result of the SPAN electrode after 650 cycles in LDEE showed no evidence of S dissolution, maintaining the same S/N ratio as the pristine electrode (Fig. S16A). As investigated by XPS, the LDEE cycled SPAN electrode displayed Li-F-rich CEI (cathode electrolyte interface), which may serve as a protective layer as well (Fig. S17C). While the 1 M LiFSI/EC-DEC and 1 M LiFSI/DEE electrolytes failed to provide stable anode and cathode performance, respectively, the LDEE was found to solve both design challenges simultaneously.

Next, we examined the performance of Li||SPAN full cells with a lithium anode of limited capacity as compared to the cathode to provide a practical battery for energy density projections. Commercial areal capacity SPAN cathodes were fabricated with an initial discharge capacity of 4.7 mAh cm^{-2} at 0.875 mA cm^{-2} in 1 M LiFSI/EC-DEC , which was matched with $40 \mu\text{m}$ thick lithium as the anode, corresponding to one-fold excess of lithium. The cell was cycled at 0.875 mA cm^{-2} 10 times before increasing the current density to 1.75 mA cm^{-2} for long term cycling. This SPAN cathode also showed increased capacity in

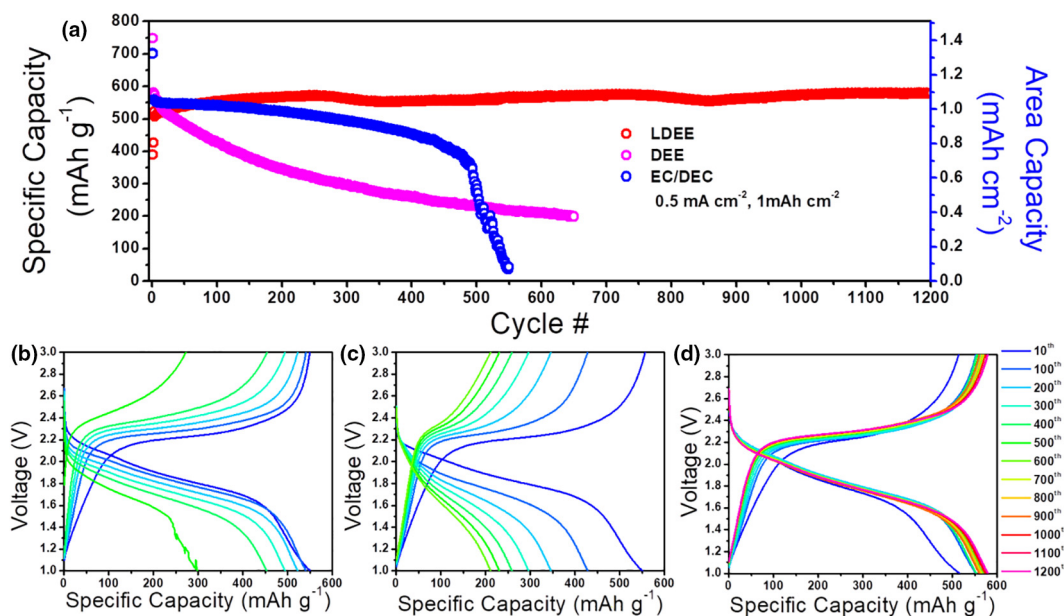


FIGURE 5

Cycling performance of Li||SPAN cells. (a) Comparison of capacities of SPAN in different electrolytes. Charge/discharge voltage profiles of SPAN: (b) in 1 M LiFSI/EC-DEC electrolyte. (c) In 1 M LiFSI/DEE electrolyte. (d) In $1.8 \text{ M LiFSI/DEE-BTFE}$ electrolyte. At 0.5 mA cm^{-2} , between 1 V and 3 V . The lithium chips are $250 \mu\text{m}$. The N/P ratio is ~ 43.2 . Flooded electrolyte is used.

LDEE at early stages of cycling (Fig. S18), and delivered a capacity of $>3.5 \text{ mAh cm}^{-2}$ at 1.75 mA cm^{-2} in both electrolytes. The Li||SPAN cell exhibited stable cycling in EC-DEC until the 25th cycle, after which the capacity dropped rapidly due to the exhaustion of excess lithium (Fig. 6a). By contrast, the limited Li||SPAN cell demonstrated stable cycling for 300 cycles in LDEE. We do observe a gradual decrease in the capacity, which is associated with the polarization increase caused by slow consumption of electrolyte (Fig. 6c) [9]. However, the CE calculated by averaging the CE from 160 cycles was found to be 99.95%, which indicates that the excess lithium was still present in the cell until this point (Fig. S19). This Li consumption rate corresponds to an actual lithium CE of 99.38% over the first 160 cycles, which was calculated to increase to 99.45% for the remainder of testing. These practical full cell tests not only verified the high CE of lithium metal in LDEE electrolyte, but also demonstrated a lithium metal battery cycled at elevated current density and areal loadings.

The morphologies of the $40 \mu\text{m}$ lithium anodes cycled with SPAN in different electrolytes were further investigated by SEM, where the lithium anode after 62 cycles (failure point of the EC-DEC system) exhibited a porous structure and clearly needle-like lithium (Fig. 7b), as well as a volume expansion to $141 \mu\text{m}$, corresponding to a porosity of 71% (Fig. 7e). In comparison, the lithium cycled in LDEE 62 times displayed lithium particles with sizes between 5 and $10 \mu\text{m}$ (Fig. 7c) and a total thickness of $51 \mu\text{m}$, including the $11 \mu\text{m}$ of uncycled pristine

lithium between the cycled lithium and Cu substrate (Fig. 7f). The studies on the morphologies of cycled lithium further confirms the CE of lithium metal in LDEE, and the densely packed lithium particle morphology in the Li||SPAN full cell.

Practical evaluation of the LDEE system

To put our results in the context of recently published work, a summary of the Li metal anode coulombic efficiencies achieved by different strategies was plotted and compared (Fig. 8, Table S2). The strategies cover the previously discussed methods: designing new electrolytes, artificial lithium surface protection, constructing 3D porous hosts, and decorating the separator. Most of the published literature reported CE values obtained at current densities between 0.5 mA cm^{-2} and 2 mA cm^{-2} , where high CE can be easily achieved. For example, a few reports presented $>99.0\%$ CE at 0.2 mA cm^{-2} and 0.25 mA cm^{-2} (Fig. 8a). Generally, as the current density increases, the lithium metal CE decreases, which is an important consideration for assessing this work (star symbols, Fig. 8a) [52]. While we report a high CE of 99.5% at a moderate current density of 0.5 mA cm^{-2} , our cells demonstrate a CE of 99.0% and 98.7% at 5 mA cm^{-2} and 10 mA cm^{-2} , respectively, which is a key metric in evaluating the electrolyte's ability to support high cathode capacities and the promise of fast charging features.

Besides the CE, the lifespan of lithium metal is another key factor for evaluating stability. Due to the discrepancies in the capacities used for cycling lithium in literature, the cumulative

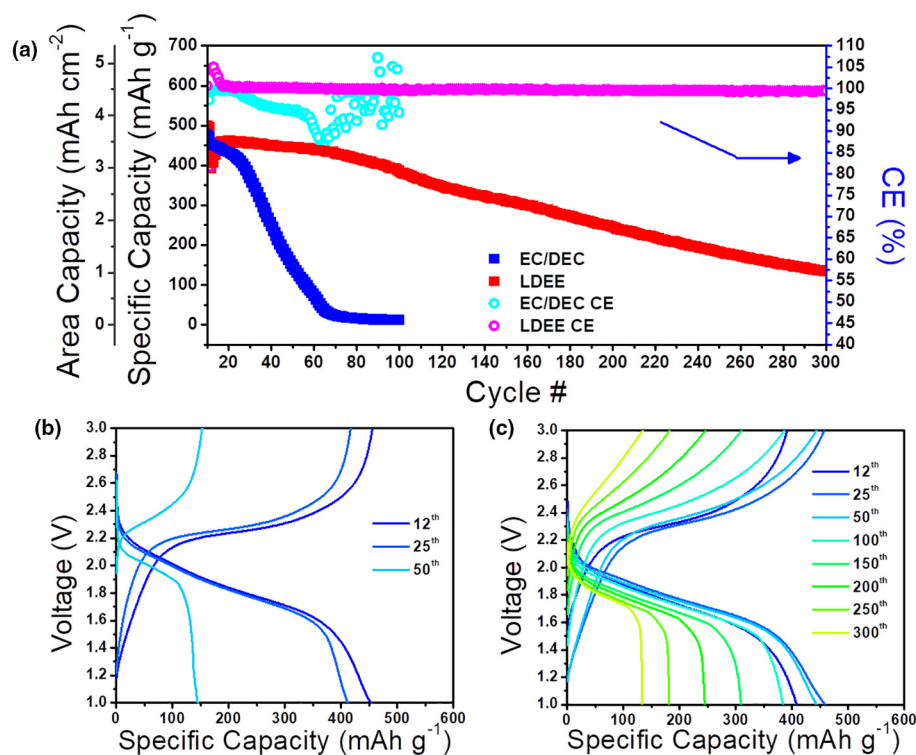


FIGURE 6

Cycling performance of limited-Li||SPAN full cells. (a) Comparison of capacities of SPAN in different electrolytes. Charge/discharge voltage profiles of SPAN: (b) in 1 M LiFSI/EC-DEC, and (c) 1.8 M LiFSI/DEE-BTFE electrolytes at 1.75 mA cm^{-2} , between 1 V and 3 V. The lithium chips are $40 \mu\text{m}$, which is one folder excess of lithium. The cell was cycled at 0.875 mA cm^{-2} for 10 times before increasing the current density to 1.75 mA cm^{-2} for long term cycling. The electrolyte amount in the cell is $\sim 9.5 \mu\text{L mAh}^{-1}$. The N/P ratio is ~ 0.95 .

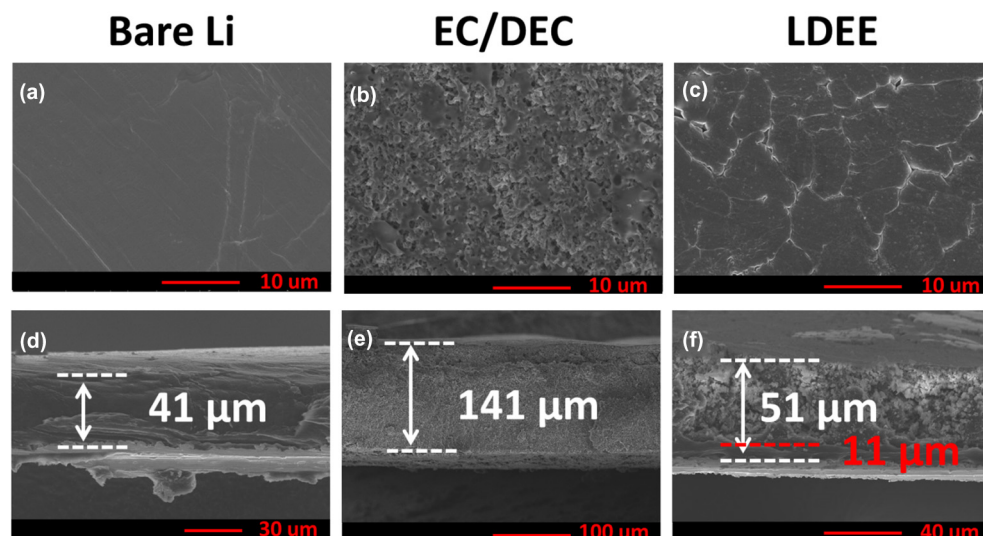


FIGURE 7

SEM images of lithium anodes. Top views: (a) Fresh lithium anode. Lithium anodes after 62 cycles in (b) 1 M LiFSI/EC-DEC, and (c) 1.8 M LiFSI/DEE-BTFE electrolytes. Cross sectional views: (d) Fresh lithium anode. Lithium anodes after 62 cycles in (e) 1 M LiFSI/EC-DEC, and (f) 1.8 M LiFSI/DEE-BTFE electrolytes. At 1.75 mA cm^{-2} , between 1 V and 3 V.

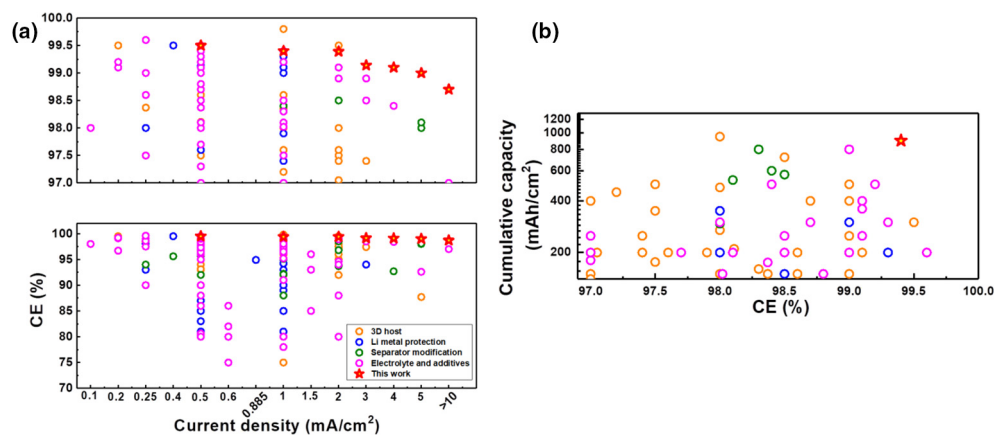


FIGURE 8

Summary of lithium metal anode coulombic efficiencies reported in literatures. (a) Average CEs at different current densities. (b) Lifespan of lithium metal anode.

capacities (capacity per cycle multiplied by cycle number) are used here for comparison (Fig. 8b, Fig. S20). This work demonstrates a CE of 99.4% and a cumulative capacity of 900 mAh cm^{-2} , the highest CE reported at such cumulative capacity to our knowledge.

Wang et al. reported SPAN with a high capacity of 694 mAh g^{-1} and an average discharge voltage of $\sim 1.8 \text{ V}$, which translates to a high energy density of 1249 Wh kg^{-1} at the material level [49,51,53]. In a real battery, both of the active materials, e.g., cathode and anode materials, and non-active materials, e.g., electrolyte, current collector, separator, conductive additive, binder, and packing materials, contribute to the weight of the battery. Therefore, the energy density of current state-of-art lithium ion batteries are $< 300 \text{ Wh kg}^{-1}$, although the cathode materials exceed 700 Wh kg^{-1} [1,2,54]. Here, we calculate a projected

energy density as a function of cathode capacity loading of our Li||SPAN system, based on the pouch cell model proposed by the Battery 500 consortium [1,54] in Fig. S21, with details of the cell design provided in Table S3. Our calculation reveals that the high electrolyte to capacity ratio (e.g., 25 g Ah^{-1} , which is commonly used in coin cell test) results in cell energy densities of $< 65 \text{ Wh kg}^{-1}$, even with a cathode loading of 9 mAh cm^{-2} . Note that the electrolyte amount in current commercial lithium ion batteries are around 1.3 g Ah^{-1} [54]. Hence, reducing the electrolyte to capacity ratio to $2\text{--}3 \text{ g Ah}^{-1}$ is a crucial next step to achieve $> 300 \text{ Wh kg}^{-1}$ Li||SPAN batteries. For example, if the electrolyte in a Li||SPAN cell is 2 g Ah^{-1} , and the cathode loading is 7.5 mAh cm^{-2} , the energy density of our cell is calculated to be 352 Wh kg^{-1} . Further optimization and cell engineering are in progress to achieve high energy density Li||SPAN pouch cells.

Conclusion

To summarize, we designed a novel ether based localized high concentration electrolyte which provided improved towards lithium metal anodes and SPAN cathodes. Computer simulations revealed that the high Li⁺ coordinated ether is thermodynamically and electrochemically stabilized. Surface analyses verify a beneficial LiF-rich SEI layer forms on the cycled Li through the salt decomposition prior to the solvent reduction. As a consequence, homogenous Li was deposited with high average CE of 99.37% for more than 900 cycles. The high CE of 98.7% has also been demonstrated at 10 mA cm⁻², indicative of the viability of the system to support high cathode loadings and fast charging operation. The constructed Li||SPAN battery with our electrolyte provided a high specific capacity of 579 mAh g⁻¹ without any degradation for 1200 cycles. In addition, the Li||SPAN battery with only one fold excess of lithium also presented cycling performance corresponding to a calculated lithium metal CE of 99.4%. This study offers an effective strategy for stabilizing both lithium metal anodes and SPAN cathodes in ether based liquid electrolyte, which is a potential solution for high energy density batteries with low cost.

Data availability

The raw/processed data required to reproduce these findings cannot be shared at this time due to technical or time limitations—the data also form part of an ongoing study.

CRedit authorship contribution statement

Haodong Liu: Conceptualization, Methodology, Formal analysis, Investigation, Writing - original draft, Visualization, Supervision, Project administration. **John Holoubek:** Methodology, Formal analysis, Validation, Investigation, Visualization. **Hongyao Zhou:** Methodology, Formal analysis, Investigation, Visualization. **Amanda Chen:** Software, Methodology. **Naijen Chang:** Software, Methodology. **Zhaohui Wu:** Resources, Investigation. **Sicen Yu:** Investigation, Visualization. **Qizhang Yan:** Investigation, Visualization. **Xing Xing:** Resources, Investigation. **Yejing Li:** Visualization. **Tod A. Pascal:** Software, Methodology, Supervision. **Ping Liu:** Conceptualization, Supervision, Project administration, Funding acquisition.

Declaration of Competing Interest

The authors declare that they have no known competing financial interests or personal relationships that could have appeared to influence the work reported in this paper.

Acknowledgments

This work was supported by the Office of Vehicle Technologies of the U.S. Department of Energy through the Advanced Battery Materials Research (BMR) Program (Battery500 Consortium) under Contract No. DE-EE0007764. Part of the work used the UCSD-MTI Battery Fabrication Facility and the UCSD-Arbin Battery Testing Facility. The authors would like to thank Dr. Ich Tran for his help with the XPS experiments at the University of California, Irvine Materials Research Institute (IMRI) using instrumentation funded in part by the National Science Founda-

tion Major Research Instrumentation Program under Grant No. CHE-1338173.

Author Contributions

H.D.L., and P.L. conceived the idea and designed the experiment. H.D.L. performed the electrochemical tests and conducted characterizations. J.H., A.C., N.C., and T.A.P. conducted the theoretical calculations. H.Z. collected the CV and conductivity data. Z.W., and X.X. contributed to the SPAN material synthesis. S.Y., and Q.Y. summarized the literature data. All authors contributed to the discussion and provided feedback on the manuscript.

Declaration of Interests

The authors declare no competing interests.

Appendix A. Supplementary data

Supplementary data to this article can be found online at <https://doi.org/10.1016/j.mattod.2020.09.035>.

References

- [1] J. Liu et al., *Nat Energy* (2019).
- [2] P. Albertus et al., *Nat. Energy* 3 (2018) 16–21.
- [3] W. Xu et al., *Energy Environ. Sci.* 7 (2014) 513–537.
- [4] K. Xu, *Chem. Rev.* 114 (2014) 11503–11618.
- [5] D. Lin, Y. Liu, Y. Cui, *Nat. Nano* 12 (2017) 194–206.
- [6] X.B. Cheng et al., *Chem. Rev.* 117 (2017) 10403–10473.
- [7] X.L. Fan et al., *Nat. Nanotechnol.* 13 (2018) 715+.
- [8] S.R. Chen et al., *Adv. Mater.* 30 (2018).
- [9] X.D. Ren et al., *Chem-US* 4 (2018) 1877–1892.
- [10] S.H. Jiao et al., *Nat. Energy* 3 (2018) 739–746.
- [11] X. Cao et al., *Nat. Energy* 4 (2019) 796–805.
- [12] X.D. Ren et al., *Joule* 3 (2019) 1662–1676.
- [13] G.M.A. Girard et al., *Batteries Supercaps* 2 (2019) 229–239.
- [14] J. Xie et al., *Batteries Supercaps* 3 (2020) 47–51.
- [15] N.W. Li et al., *Adv. Mater.* 28 (2016) 1853–1858.
- [16] B.-S. Lee et al., *ACS Appl. Mater. Interfaces* 10 (2018) 38928–38935.
- [17] H. Zhou et al., *J. Power Sources* 450 (2020) 227632.
- [18] H.D. Liu et al., *ACS Appl. Energy Mater.* 1 (2018) 1864–1869.
- [19] X. Ke et al., *Energy Storage Mater.* (2019).
- [20] H. Liu et al., *Energy Storage Mater.* 16 (2019) 505–511.
- [21] C.J. Niu et al., *Nat. Nanotechnol.* 14 (2019). 594+.
- [22] L.M. Suo et al., *Science* 350 (2015) 938–943.
- [23] J.F. Qian et al., *Nat. Commun.* 6 (2015).
- [24] S.R. Chen et al., *Joule* 2 (2018) 1548–1558.
- [25] B.D. Adams et al., *Adv. Energy Mater.* 8 (2018).
- [26] X. Lin et al., *Carbon Energy* 1 (2019) 141–164.
- [27] J. Wu et al., *Carbon Energy* 1 (2019) 57–76.
- [28] Z. Yan, H. Jin, J. Guo, *Carbon Energy* 1 (2019) 246–252.
- [29] Y. Yuan, J. Lu, *Carbon Energy* 1 (2019) 8–12.
- [30] G.A. Kaminski et al., *J. Phys. Chem. B* 105 (2001) 6474–6487.
- [31] J.N. Canongia Lopes, J. Deschamps, A.A.H. Pádua, *J. Phys. Chem. B* 108 (2004) 2038–2047.
- [32] L.X. Dang, *J. Chem. Phys.* 96 (1992) 6970–6977.
- [33] C. Park et al., *J. Power Sources* 373 (2018) 70–78.
- [34] S. Plimpton, *J. Comput. Phys.* 117 (1995) 1–19.
- [35] W. Shinoda, M. Shiga, M. Mikami, *Phys. Rev. B* 69 (2004) 134103.
- [36] G.J. Martyna, D.J. Tobias, M.L. Klein, *J. Chem. Phys.* 101 (1994) 4177–4189.
- [37] M. Parrinello, A. Rahman, *J. Appl. Phys.* 52 (1981) 7182–7190.
- [38] M.E. Tuckerman et al., *J. Phys. A: Math. Gen.* 39 (2006) 5629–5651.
- [39] T.A. Pascal, S.-T. Lin, W.A. Goddard III, *PCCP* 13 (2011) 169–181.
- [40] S.-T. Lin, M. Blanco, W.A. Goddard, *J. Chem. Phys.* 119 (2003) (1805) 11792–11801.
- [41] M.S. Green, *J. Chem. Phys.* 22 (1954) 398–413.
- [42] R. Kubo, M. Yokota, S. Nakajima, *J. Phys. Soc. Jpn.* 12 (1957) 1203–1211.
- [43] Y. Shao et al., *Mol. Phys.* 113 (2015) 184–215.
- [44] L.M. Suo et al., *Proc. Natl. Acad. Sci. U.S.A.* 115 (2018) 1156–1161.

- [45] X.L. Fan et al., *Chem-Us* 4 (2018) 174–185.
- [46] X. Xing et al., *Energy Storage Mater.* (2019).
- [47] Y. Lin et al., *Batteries Supercaps* 2 (2019) 774–783.
- [48] W. Shin, J. Lu, X. Ji, *Carbon Energy* 1 (2019) 165–172.
- [49] S.Y. Wei et al., *J. Am. Chem. Soc.* 137 (2015) 12143–12152.
- [50] Z.Q. Jin et al., *Energy Storage Mater.* 14 (2018) 272–278.
- [51] H.J. Yang et al., *Energy Storage Mater.* 15 (2018) 299–307.
- [52] S.H. Jiao et al., *Joule* 2 (2018) 110–124.
- [53] J.L. Wang et al., *Adv. Funct. Mater.* 23 (2013) 1194–1201.
- [54] S. Chen, et al., *Joule*.